

# Topological properties of the mesoscopic graphene plaquette: QSHE due to spin imbalance

B. Ostahie<sup>1,2</sup>, M. Niță<sup>1</sup> and A. Aldea<sup>1</sup>

<sup>1</sup> *National Institute of Materials Physics,*

*POB MG-7, 77125 Bucharest-Magurele, Romania*

<sup>2</sup> *Faculty of Physics, University of Bucharest, Romania*

(Dated: February 17, 2014)

## Abstract

We study the electronic properties of the confined honeycomb lattice in the presence of the intrinsic spin-orbit (ISO) interaction and perpendicular magnetic field, and report on uncommon aspects of the quantum spin Hall conductance corroborated by peculiar properties of the edge states. The ISO interaction induces two specific gaps in the Hofstadter spectrum, namely the 'weak' topological gap defined by Beugeling *et al* [Phys. Rev. B **86**, 075118 (2012)], and spin-imbalanced gaps in the relativistic range of the energy spectrum. We analyze the evolution of the helical states with the magnetic field and with increasing Anderson disorder. The 'edge' localization of the spin-dependent states and its dependence on the disorder strength is shown. The quantum transport, treated in the Landauer-Büttiker formalism, reveals interesting new plateaus of the quantum spin Hall effect (QSHE), and also of the integer quantum Hall effect (IQHE), in the energy ranges corresponding to the spin-imbalanced gaps. The properties of the spin-dependent transmittance matrix that determine the symmetries with respect to the spin, energy and magnetic field of the longitudinal and transverse resistance are shown.

PACS numbers: 73.23.-b, 73.43.-f, 72.80.Vp, 73.22.Pr

## I. INTRODUCTION

The large conceptual interest for the properties of graphene was motivated first by the relativistic-like effects in the honeycomb structure and the opportunity for the high temperature relativistic integer quantum Hall effect [1]. Next, the interest was also stimulated by the topological insulating properties, based on the helical edge states of graphene, that support the quantum spin Hall effect (QSHE). The topological phase of the graphene, predicted by Kane and Mele [2], is induced by the *intrinsic* spin-orbit (ISO) coupling, which opens a *topological gap* between the Dirac cones located at the points  $K$  and  $K'$  in the Brillouin zone. The gap is filled with helical states stretching along the edges, which appear in pairs and carry opposite spins in opposite directions. One has to remind that the helical states are protected against disorder by the time-reversal symmetry of the Hamiltonian, but they are not protected against the spin-flip processes involved by the Rashba-type coupling or against a staggered sublattice potential; a phase diagram can be theoretically obtained in the space of the coupling parameters corresponding to the different interactions [3].

Because of the very small spin-orbit coupling, the QSHE could not be proved experimentally in graphene. The experimental endeavor moved toward other 2D systems which show topological properties, like CdTe/HgTe/CdTe [4–6] or AlSb/InAs/GaSb/AlSb [7, 8] quantum wells, and toward the 3D topological insulators [9, 10]. The honeycomb lattice remains however under investigation, as optical and synthetic such lattices (where the magnetic flux and the spin-orbit coupling strength can be artificially tuned) were obtained [11, 12]. Another line of investigation consists in finding techniques for the enhancement of the spin-orbit coupling by introducing adatoms in graphene [13, 14] or using other 2D materials like silicene [15, 16].

When discussing different topological systems, attention should be paid to the existence and behavior of the different types of edge states (helical or chiral), which depend on various factors as the lattice structure, geometry of the sample, spin-orbit interaction, presence of the magnetic field. We remind, for instance, that even for vanishing spin-orbit interaction, edge states are supported by the zig-zag graphene ribbon, but not by the arm-chair ribbon. This was proved by solving the Dirac equation with proper boundary conditions [17] or by calculating the Zak invariant [18]. However, when the intrinsic spin-orbit coupling is considered, the edge states, which become now spin-polarized and helical, are present both in the

zig-zag [2] and arm-chair [19] ribbons. The relevance of the sample geometry can be noticed also by unfolding the ribbon and imposing everywhere vanishing boundary conditions. For the finite-size plaquette, we find that the helical edge states extend all around the perimeter, looking however different along the zig-zag and arm-chair margin, respectively (see Fig.2).

When the system is subject to a magnetic field, which breaks the time-reversal symmetry, we expect interesting peculiarities of the edge states under the mixed effect of the magnetic field and spin-orbit (SO) interaction. Even for the torus geometry (i.e., with periodic boundary conditions along the both directions), when the edge states are missing, the Hofstadter energy spectrum exhibits relevant aspects in the simultaneous presence of the intrinsic SO coupling, Rashba-type SO interaction and perpendicular magnetic field [20]. It turns out that the topological gap opened around  $E = 0$  [21] closes with increasing magnetic flux, and it is *weak* in the sense that it is annihilated by the Rashba coupling. It was also found in the graphene ribbon subjected to a magnetic field that an additional staggered potential [22] induces spin imbalanced regions in the spectrum, where the number of spin-up and spin-down states are different [20]. For the confined graphene system, a spin imbalance will be detected in this paper as due to the splitting induced by the ISO coupling, and interesting consequences for the charge and spin transport will be put forward.

In this paper we study the confined honeycomb lattice obtained by imposing vanishing boundary conditions all along the perimeter. This approach simulates the mesoscopic case, provides some specific new properties, and allows for the calculation of the transport properties and disorder effects. The plaquette exhibits both zig-zag and arm-chair boundaries as in Fig.1, and the first question concerns the fate of the helical states familiar from the cylinder (ribbon) geometry. The combined effect of the intrinsic SO coupling and perpendicular magnetic field on the spectral properties of the graphene plaquette are discussed in the next section. Some specific spectral properties anticipate new aspects of the charge and spin transport, which are presented in section III. The robustness of the spectral properties against the Anderson disorder is analyzed in a subsection. The disordered spectrum corresponding to helical states exhibits a tulip-like picture due to existence in the graphene spectrum of some highly degenerated energies (corresponding to the saddle points in the infinite model). In section III we show how the symmetry properties of the spin-dependent electron transmittance give rise to particular features of the charge and spin currents, which are calculated in the Landauer-Büttiker formalism for a four-lead device. Both the spin

and charge Hall conductance exhibit supplementary plateaus corresponding to gaps characterized by the imbalance between the edge states with opposite spins. The conclusions are summarized in the last section.

## II. SPECTRAL PROPERTIES OF THE TOPOLOGICAL INSULATING GRAPHENE PLAQUETTE IN MAGNETIC FIELD

In this section we reveal new spectral properties of topological graphene in perpendicular magnetic field, insisting on the features of the different types of edge states that result by imposing vanishing boundary conditions all around the perimeter of the plaquette. The localization of the wave function and the robustness against disorder are discussed.

We remind that the Hofstadter spectrum of the graphene sheet in the absence of the spin-orbit coupling looks like a double butterfly [23, 24], and exhibits both relativistic Dirac-Landau bands in the middle and conventional Bloch-Landau bands at the extremities of the spectrum [25], separated by well-defined gaps. In the case of the *finite* plaquette, the vanishing boundary conditions and the perpendicular magnetic field generate *chiral* edge states that fill the gaps. The sign of chirality is determined by the direction of the magnetic field, and one has to mention that the relativistic and conventional edge states show opposite chirality. A second class of edge states in the system are the *helical* ones, which appear in the presence of the ISO coupling, and are located in the topological gap opened by this interaction.

Our aim in this section is: i) to note the evolution of the helical states with the magnetic field, ii) to evaluate the degree of localization along the edges of the helical and chiral states, iii) to identify domains of imbalance between the densities of spin-up and spin-down edge states (where the charge and spin currents should become anomalous), iv) to see the effect of the Anderson disorder on the energy spectrum and on the 'edge' localization of helical states.

Adopting the tight-binding representation, as the 2D honeycomb lattice contains two atoms  $A$  and  $B$  per unit cell, we define corresponding creation and annihilation operators  $a_{\sigma,nm}^\dagger, b_{\sigma,nm}^\dagger, a_{\sigma,nm}, b_{\sigma,nm}$ , where  $\sigma = \pm 1$  is the spin index and  $\{n, m\}$  are the cell indices (see

Fig.1). The Hamiltonian defined on the honeycomb lattice can be written as:

$$H = \sum_{\sigma} H_0^{\sigma} + \sum_{\sigma} H_{SO}^{\sigma} , \quad (1)$$

where the first term describes the tunneling between the nearest neighbors, while the second one represents the intrinsic spin-orbit interaction. In the presence of a perpendicular magnetic field, described by the vector potential  $\vec{A} = (-By, 0, 0)$ , the first term reads:

$$H_0^{\sigma} = \sum_{nm} E_a a_{\sigma,nm}^{\dagger} a_{\sigma,nm} + E_b b_{\sigma,nm}^{\dagger} b_{\sigma,nm} + t(e^{i\phi(m)} a_{\sigma,nm}^{\dagger} b_{\sigma,nm} + e^{i\phi(m)} b_{\sigma,n+1,m}^{\dagger} a_{\sigma,nm} + b_{\sigma,n,m+1}^{\dagger} a_{\sigma,nm} + H.c.). \quad (2)$$

$E_{a,b}$  are the atomic energies,  $t$  is the hopping integral between the sites  $A$  and  $B$ , and the Peierls phase due to the magnetic field equals  $\phi(m) = \pi(m + \frac{1}{6})\Phi$ , where the magnetic flux through the unit cell  $\Phi$  is expressed in quantum flux units  $\Phi_0 = h/e$ .

The intrinsic spin-orbit Hamiltonian [2] conserves the electron spin  $S_z$ , and invokes the hopping to the six next-nearest-neighbors, keeping also in mind the chirality of the trajectory between the two sites. In the presence of the magnetic field, the hopping terms acquire a supplementary phase, and the Hamiltonian can be written in a compact form as [19]:

$$H_{SO}^{\sigma} = i\lambda_{SO} \frac{1}{2} \sigma \sum_{\langle\langle nm, n'm' \rangle\rangle} \nu_{nm} e^{i\phi_{nm}^a} a_{\sigma,n'm'}^{\dagger} a_{\sigma,nm} + (a \rightarrow b) + H.c. , \quad (3)$$

where  $\lambda_{SO}$  is the spin-orbit coupling constant,  $\nu_{nm} = \pm 1$  expresses the clock- or anticlockwise chirality of the trajectory between the next-nearest-neighbors, and the phases  $\phi_{nm}^a, \phi_{nm}^b$  should be calculated by the integration of the vector potential along each trajectory. The Hamiltonian (3) contains many terms and, for the reader's sake, we write it in detail, and show also the illustrative Fig.1 :

$$\begin{aligned} H_{SO}^{\uparrow} &= i\lambda_{SO} \frac{1}{2} \sum_{nm} e^{i\phi_1^a(m)} a_{\uparrow,n,m+1}^{\dagger} a_{\uparrow,n,m} + e^{i\phi_2^a(m)} a_{\uparrow,n+1,m-1}^{\dagger} a_{\uparrow,n,m} + e^{i\phi_3^a(m)} a_{\uparrow,n-1,m}^{\dagger} a_{\uparrow,n,m} \\ &\quad + e^{i\phi_1^b(m)} b_{\uparrow,n+1,m}^{\dagger} b_{\uparrow,n,m} + e^{i\phi_2^b(m)} b_{\uparrow,n-1,m+1}^{\dagger} b_{\uparrow,n,m} + e^{i\phi_3^b(m)} b_{\uparrow,n,m-1}^{\dagger} b_{\uparrow,n,m} + H.c. , \\ H_{SO}^{\downarrow} &= -i\lambda_{SO} \frac{1}{2} \sum_{nm} e^{-i\phi_1^a(m)} a_{\downarrow,n-1,m+1}^{\dagger} a_{\downarrow,n,m} + e^{-i\phi_2^a(m)} a_{\downarrow,n,m-1}^{\dagger} a_{\downarrow,n,m} + e^{-i\phi_3^a(m)} a_{\downarrow,n+1,m}^{\dagger} a_{\downarrow,n,m} \\ &\quad + e^{-i\phi_1^b(m)} b_{\downarrow,n-1,m}^{\dagger} b_{\downarrow,n,m} + e^{-i\phi_2^b(m)} b_{\downarrow,n+1,m-1}^{\dagger} b_{\downarrow,n,m} + e^{-i\phi_3^b(m)} b_{\downarrow,n,m+1}^{\dagger} b_{\downarrow,n,m} + H.c.. \end{aligned} \quad (4)$$

The phases in the above equation are the following:

$$\begin{aligned}\phi_1^a(m) &= \pi(m + \frac{5}{6})\Phi, \quad \phi_2^a(m) = \pi(m - \frac{1}{6})\Phi, \quad \phi_3^a(m) = -2\pi(m + \frac{1}{3})\Phi, \\ \phi_1^b(m) &= 2\pi m\Phi, \quad \phi_2^b(m) = -\pi(m + \frac{1}{2})\Phi, \quad \phi_3^b(m) = -\pi(m - \frac{1}{2})\Phi.\end{aligned}\quad (5)$$

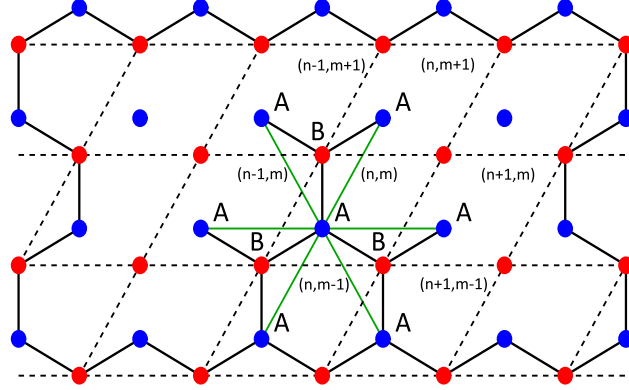


FIG. 1: (Color online) The sketch of the graphene plaquette with horizontal zig-zag and vertical arm-chair edges. The two type of atoms in the unit cell are A (blue) and B (red);  $(n,m)$  are the cell indices. The green lines connect an atom A to the six next-nearest neighbors, while the nearest neighbors are connected by black lines; the units cells are drawn with dashed lines. The number of lattice sites is  $11 \times 4$ .

It is worth to note some symmetry properties of the energy spectrum. Since the Hamiltonian (1) commutes with  $S_z$ , its spectrum is the union of the spin-up and spin-down eigenvalues  $\{E_i\} = \{E_n^\uparrow\} \cup \{E_n^\downarrow\}$ , where  $n = 1, \dots, N$  ( $N$  being the total number of sites on the finite lattice). Let  $n = 1$  be the index of the lowest eigenvalue for both spin-up and spin-down subsets. With this notation, the symmetry of the Hamiltonian (1) generates the property  $E_n^\uparrow(\Phi) = -E_{N+1-n}^\downarrow(\Phi)$ . In words, this means that if the energy  $E$  belongs to the spin-up subset of the spectrum, the energy  $-E$  exists also in the spectrum, but belongs to the spin-down subset. One has also to note that the usual periodicity with the magnetic flux  $E_i(\Phi) = E_i(\Phi + \Phi_0)$ , which is valid at  $\lambda_{SO} = 0$ , is replaced by  $E_i(\Phi) = E_i(\Phi + 6\Phi_0)$  in the case of non-vanishing spin-orbit coupling [20].

An eigenfunction of the Hamiltonian (1) with  $\Phi = 0$  corresponding to a helical edge state is shown in Fig.2. It is to observe that the state stretches along the whole perimeter of the

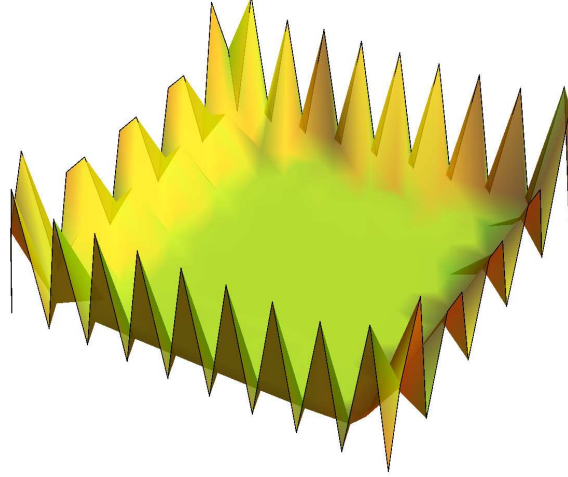


FIG. 2:  $|\Psi(r)|^2$  for a helical state on the graphene plaquette at  $\Phi = 0$  and  $\lambda_{SO} = 0.2$ ; a different aspect along the two different edges (zig-zag and arm-chair) is noticed. The number of lattice sites is  $19 \times 10$ .

plaquette, but the aspect along the zig-zag edges differs from that one along the arm-chair edges.

#### A. Edge states in the 'weak' topological gap

For vanishing SO coupling, the low flux range of the Hofstadter butterfly of the finite-size graphene plaquette shows a thin, quasi-degenerate band at  $E = 0$ , as it can be noticed in Fig.3(left). These states correspond to the Landau band indexed by  $n = 0$  in the periodic geometry, and their number depends on the dimension of the plaquette. The significant changes that appear when the ISO coupling is introduced are only partially studied in the presence of the magnetic field. One knows that the topological gap existing at  $\Phi = 0$  persists at low flux, but closes with increasing  $\Phi$ . This gap is called 'weak' in [20], and we keep the terminology. However, the origin and properties of the edge states filling the weak topological gap of the mesoscopic graphene plaquette have not been studied yet. They result from the simultaneous presence of the magnetic field and ISO interaction, and have to justify the survival of the QSHE at non-vanishing magnetic field (see Fig.12).

The analysis of the edge states located in the topological gap will be done by inspection of Fig.3(right) and Fig.4. One may identify a first class of states resulting from the splitting

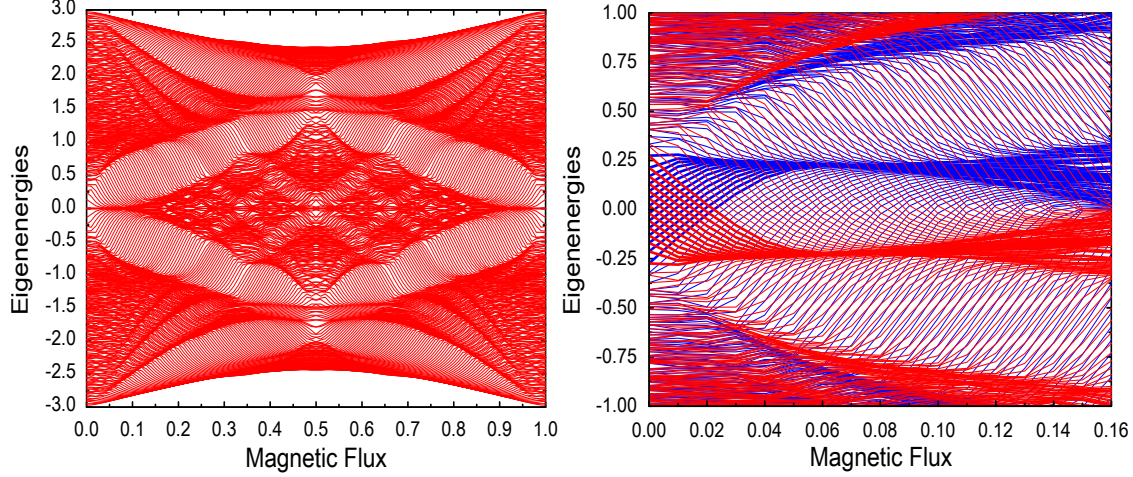


FIG. 3: (Color online)(left) The Hofstadter spectrum of the finite graphene lattice in the absence of the SO coupling; due to confinement, the gaps are filled with edge states. (right) The central part of the energy spectrum showing the weak topological gap and two adjacent relativistic gaps in the presence of the ISO coupling. The spin-up eigenvalues are colored in red, while the spin-down in blue. The energy is measured in units of hopping integral  $t$ , the magnetic flux in flux quanta  $\Phi_0$ , and  $\lambda_{SO} = 0.05$ . The number of lattice sites is  $21 \times 20$ .

in magnetic field of the doubly-degenerated helical states existing at  $\Phi = 0$ . These states are drawn in Fig.3(right) with thicker lines. One notices that at low flux the splitting that separates the spin-up and the spin-down levels increases linearly with  $\Phi$ , however, at some higher magnetic flux, all these states merge into bands that border the weak topological gap (colored in red for spin-up and blue for spin-down). Since  $dE^\uparrow/d\Phi$  and  $dE^\downarrow/d\Phi$  show opposite signs, the states of opposite spins continue to carry opposite spin currents. Besides, the weak topological gap accommodates also a second category of edge states, which are chiral states stemming from the adjacent relativistic gaps. We can see, for instance, that spin-down states (in blue) coming from the relativistic gap below cross the red band (composed of spin-up states), enter the weak topological gap, and eventually merge the blue band that border the topological gap from above (and similarly for the spin-up red lines entering the topological gap from above).

The both types of edge states filling the weak topological gap at  $\Phi \neq 0$ , although of different provenance (helical or chiral), show opposite currents for opposite spins, so that the QSHE survives at any magnetic field as far as the gap remains open.



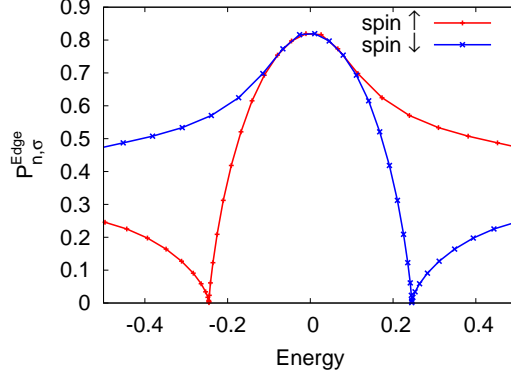


FIG. 4: Edge localization  $P_{n,\sigma}^{Edge}$  of the spin-dependent eigenenergies in the range of topological and relativistic gaps. ( $\Phi = 0.03\Phi_0$ ,  $\lambda_{SO} = 0.05$ , the number of lattice sites is  $35 \times 20$ ).

In what follows we examine the degree of localization of different edge states. The information regarding the edge localization can be obtained from the quantity:

$$P_{n,\sigma}^{Edge} = \sum_{i \in Edge} |\Psi_{n,\sigma}(i)|^2, \quad (6)$$

where the sum is taken over all sites  $i$  that belong to the plaquette boundary [26]. The data in Fig.4, calculated at  $\Phi = 0.03$ , indicate that the states that are close to  $E = 0$  are strongly localized along the edges. This is expected, but it is less expected that the helical states that converge toward the bands confining the weak topological gap at  $E \approx \pm 0.25$  are pushed away from edges, such that  $P^{edge}$  eventually vanishes at the respective energies. This denotes that, while evolving into the two bands, the helical states lose their localized character and become more similar to bulk states.

The same Fig.4 shows that outside the topological gap, in the relativistic gaps where all states are of chiral-type, the edge localization depends significantly on the spin orientation. At the same time, from Fig.3(right) one can see that the derivative  $dE_n^\sigma/d\Phi$  is also spin-dependent. At  $E > 0.25$ , for instance, both the edge localization and the magnetic moment of the spin-up states are higher than for the opposite spin.

## B. Spin-orbit effects on the properties of the relativistic gaps

A small spin-orbit coupling (meaning  $\lambda_{SO} \ll t$ ) affects visible only the center of the spectrum occupied by the topological gap and relativistic bands and gaps. The extremities

of the spectrum, corresponding to the conventional Landau bands/gaps, being less sensitive to the spin-orbit coupling. This statement is proved by Fig.5, which shows eigenvalues  $E_n^\uparrow, E_n^\downarrow$  and their corresponding index  $n$ , at a given flux. The (quasi) horizontal lines correspond to the energy gaps (where the edge states are rare) and the steps correspond to the bands (where the bulk states are dense). The difference between the two lines corresponding to opposite spins is well visible in the energy range  $[-1,1]$ , while for energies outside this range the lines overlap, meaning an indistinguishable spin-orbit splitting.

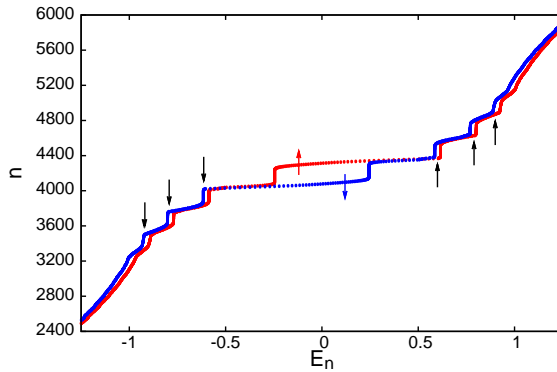


FIG. 5: The eigenvalue spectrum  $\{E_n^\sigma\}$  of the Hamiltonian (1) with  $\Phi = 0.03\Phi_0$  and  $\lambda_{SO} = 0.05$  for the finite honeycomb lattice with  $105 \times 40$  sites. The spin-up energies are shown in red, the others in blue. The black arrows indicate the presence of the spin imbalanced gaps.

We have to make two observations concerning the behavior of the spin-dependent edge states in the relativistic gaps: i) in contradistinction to the case of the topological gap (described in the previous subsection) the chirality  $dE_n^\sigma/d\Phi$  of edge states shows now the same sign, independently of the spin orientation. A difference appears however in what concerns the magnitude of the derivative, which again is more pronounced for the internal gaps and less evident at higher energies. ii) The Hofstadter butterfly exhibits the splitting of each relativistic band in two spin-dependent subbands. The small spin-orbit gap created inbetween is filled with edge states of both spin, however, essentially, the number of spin-up states differs from the number of states with spin-down. This denotes the existence in the energy spectrum of 'spin-imbalanced' gaps induced by the ISO coupling [27]. This finding should not be overlooked as it is associated obviously with an imbalance of the spin currents,

which may account for a non-zero QSHE in the corresponding energy range. The explicit calculation in the next section of the spin-dependent electron transmittance confirms this prediction.

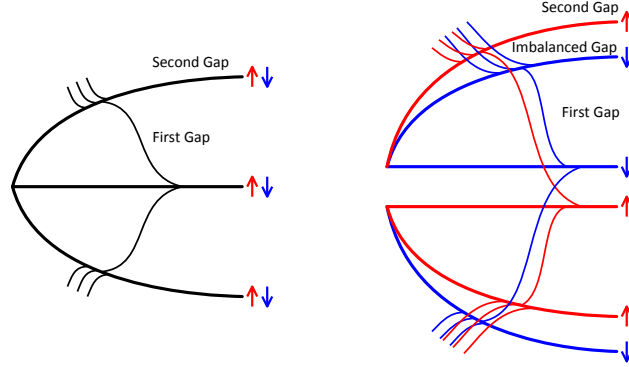


FIG. 6: (Color online) Schematic representation of the Dirac-Landau bands as function of the magnetic field: (left) in the absence of ISO coupling the bands are spin-degenerate; (right) in the presence of ISO coupling each band splits into subbands of opposite spin. The gap created in between contains a different number of spin-up and spin-down states, as explained in the text.

The sketch in Fig.6 describes the manner in which the imbalanced gap arises. On the left, we show the first two relativistic gaps, separated by the relativistic band, in the case of vanishing ISO coupling, when all states are spin-degenerate. It is known that the number of edge states crossing the Fermi level at a given flux in the first relativistic gap is  $N_{\uparrow} + N_{\downarrow} = 2$  [28], while in the second gap the number is 6. In the right panel, the degeneracy of the band and of the edge states is lifted in the presence of the ISO coupling, and a small spin-orbit gap arises between the spin-down (blue) and spin-up (red) subbands. Now, we are interested in the number and the spin of the edge states occurring in this gap. To this aim, considering, for instance, the upper half of the spectrum, let us notice that the spin-up (red) edge state crosses the spin-down subband (blue) and enter the spin-orbit gap. (At the same time, the spin-down edge state is absorbed in the subband of the same spin.) Next, we notice that three spin-down edge states originating from the blue subband emerges in the spin-orbit gap, then cross the subband of opposite spin (red), and eventually enter the second relativistic gap. Altogether, it turns out that there are four edge states in the gap we look at, namely  $N_{\uparrow} = 1$  and  $N_{\downarrow} = 3$ , fact that justifies the term of 'spin-imbalanced' gap (see also the note [29]).

### C. Disorder effects

Both the helical and chiral edge states are topological states which are robust with respect to disorder, being protected however by different symmetries. The helical states are protected by the time-reversal symmetry (TRS) which is preserved by the ISO interaction, while the chiral edge states, despite the TRS breaking, are robust against disorder due to the strong magnetic field that imposes the chiral motion and impedes the backscattering. So, it is pertinent to ask whether the two types of states are equally robust. Up till now, we could not give a definite answer to this question, and here we restrict ourselves to follow the evolution with the disorder of the spectral properties only at  $\Phi = 0$ . We use the Anderson disorder model characterized by the parameter  $W$  defining the width of the diagonal disorder.

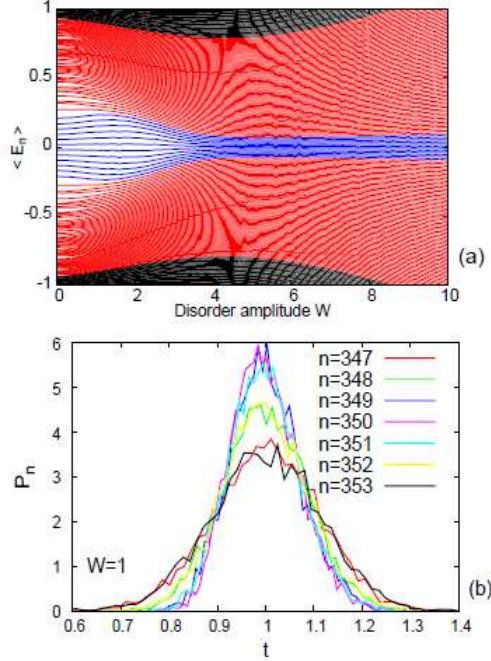


FIG. 7: (Color online) (a) Disorder averaged eigenenergies  $\langle E_n \rangle$  vs. the Anderson disorder amplitude  $W$  at  $\Phi = 0$ . The topological states (indexed by  $n \in [345, 356]$ ) are colored in blue and develop a *tulip*-like shape with increasing disorder. (b) The level spacing distribution  $P_n(t)$  for the helical states with  $n = 347, \dots, 353$  at  $W = 1$ . The distribution functions are well fitted by Gaussian functions; note that the states in the middle of the topological gap show a narrower Gaussian ( $\lambda_{SO} = 0.05$ , number of lattice sites is  $35 \times 20$ , number of disorder configurations is 880 (a) and 5000 (b)).

The general aspect of the disordered spectrum of the confined graphene lattice shown in Fig.7a is determined by the existence of regions that respond differently to the increase of the disorder strength. One knows that, at low disorder, the topological gap is not affected, but, on the other hand, the energy ranges with very high density of states about  $E = \pm 1$  (which correspond in the periodic model to the saddle points  $M$  in the Brillouin zone) are very sensitive to any disorder. The consequence is a specific *tulip*-like shape of the spectrum in the topological range  $E \in [-0.25, 0.25]$ , depicted in blue in Fig.7a. The qualitative explanation of this shape is the following: the disordered potential broadens the very dense spectrum close to  $E = \pm 1$ , where the level spacing increases with the disorder strength  $W$  and produces a 'compression' on the topological levels located in the middle of the spectrum. Since, according to the von Neumann-Wigner theorem [30, 31], the energy levels cannot cross each other, the result is the tulip shape of the levels in the topological range.

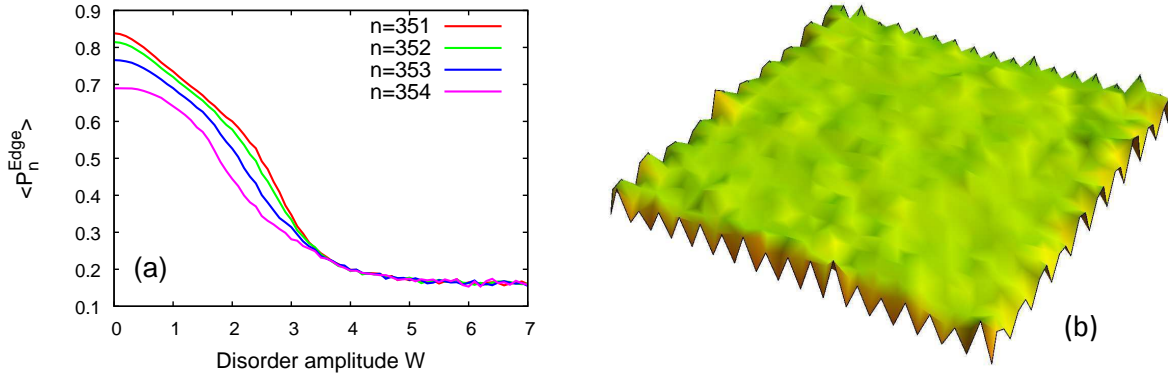


FIG. 8: (Color online) (a) The disorder averaged edge localization  $\langle P_n^{Edge} \rangle$  vs. the disorder amplitude  $W$  for several helical states; the states prove to be robust against disorder only for small disorder ( $\Phi = 0$ ,  $\lambda_{SO} = 0.05$ , no. of lattice sites is  $35 \times 20$ , no. of disorder configurations is 880). (b) The disorder averaged wave function  $\langle |\Psi(r)|^2 \rangle$  for a former helical state at  $\Phi = 0$  ( $\lambda_{SO} = 0.05$ ,  $W = 5$ , no. of lattice sites is  $35 \times 20$ , no. of disorder configurations is 500).

The level spacing analysis helps also to understand the disorder effects on the energy spectrum. Let us define the level spacing as  $t_n = \delta E_n / \langle \delta E_n \rangle$ , where  $\delta E_n = E_{n+1} - E_n$  and  $\langle \dots \rangle$  means the average over all disorder configurations. The level spacing distributions  $P_n(t)$  calculated numerically at low disorder for several  $n$ -s corresponding to states in the

topological gap are shown in Fig.7b. The distributions can be well fitted with Gaussian functions. Since the same distribution is exhibited also by the edge states in the integer quantum Hall phase [32], one may conclude that the Gaussian distribution of the level spacing is the feature of the states that are robust against disorder. It is to note in Fig.7b that the curves show different widths, namely the states in the center of the topological gap exhibit a narrower width (being more robust) than those located near the gap margin.

Additional information can be obtained by calculating the edge localization Eq.(6) as function of  $W$ . In Fig.8a we find that the disordered helical states remain localized near edges as long as  $W$  is small. However,  $P^{Edge}$  falls down with increasing disorder, meaning that the states extend gradually inside the plaquette, and eventually become disordered metallic-like states spread over the whole plaquette area if  $W \gtrsim 4$ . An example of such a uniformly distributed state originating from a helical state is shown in Fig.8b. Of course, the level spacing distribution should change also from the Gaussian to a Wigner- Dyson distribution, however this topic will be discussed elsewhere.

### III. SPECIFIC IQHE AND QSHE OF THE CONFINED GRAHENE WITH SPIN-ORBIT COUPLING

In this section, we simulate a four-lead device by attaching leads to a graphene plaquette, and calculate the longitudinal and transverse resistances corresponding to both spin and charge currents. We emphasize specific properties of the transmittance matrix  $T_{\alpha\beta}^{\sigma}$  in the presence of the ISO coupling that generate a uncommon behavior of the spin and charge quantum Hall effect. We find that, besides the usual plateaus of the Hall conductance at  $\pm(2e^2/h)(2n+1)$ , the IQHE gets new intermediate plateaus at  $\pm(2e^2/h)(2n+2)$  with  $n = 0, 1, 2, \dots$ . Next, we find that these plateaus are associated with a non-vanishing quantum spin conductance  $G_H^S = -2e/4\pi$ , the sign being opposite to the usual spin Hall conductance that occurs in the topological gap. The changes of both IQHE and QSHE can be observed in Fig.12, which represents the main result of the section. These transport effects have not been explored up till now, and it turns out that they shows up in energy gaps with spin imbalance, where  $T_{\alpha,\alpha+1}^{\uparrow} \neq T_{\alpha,\alpha+1}^{\downarrow}$ . The transport calculations are based on the Landauer-Büttiker formalism.

### A. Properties of the spin-resolved transmittances

The Landauer-Büttiker approach requires that the Hamiltonian (1) be completed with terms describing the leads ( $H_L$ ) and the coupling between leads and the graphene plaquette ( $H_{LP}$ ). Then the total Hamiltonian reads:

$$H^T = H + H_L + \tau H_{LP}, \quad (7)$$

where the last two terms are considered to be spin independent. The quantities which enter the expression of the spin-dependent electron transmittance between the leads  $\alpha$  and  $\beta$  are the lead-plaquette coupling  $\tau$ , the matrix element of the retarded Green function corresponding to the total Hamiltonian Eq.(7) and the lead density of states:

$$T_{\alpha\beta}^\sigma(E, \Phi) = 4\tau^4 |G_{\alpha\beta}^\sigma|^2(E, \Phi) \text{Im}g_\alpha^L(E) \text{Im}g_\beta^L(E), \quad \alpha \neq \beta, \quad (8)$$

where  $g^L$  is the Green function of leads. The symmetries of the energy spectrum, discussed in the previous section, determine the properties of the Green function  $G_{\alpha\beta}^\sigma$ , and reflect eventually, via Eq.(8), in the symmetries of the spin-resolved transmittance matrix:

$$T_{\alpha\beta}^\sigma(E, \Phi) = T_{\beta\alpha}^{-\sigma}(-E, \Phi) = T_{\beta\alpha}^{-\sigma}(E, -\Phi). \quad (9)$$

An inspection of the Hofstadter spectrum shows that the gaps located in the central part of the spectrum (i.e., topological and relativistic gaps) open at lower magnetic fluxes in comparison with the conventional Landau gaps located at higher energies. That is, it is hard to find a magnetic flux that allows to evidenciate simultaneously all the types of edge states occuring in different energy gaps. Intending to compare all the three regimes (topological, relativistic and conventional Landau), we need to perform the calculations at a relatively small flux, and we select  $\Phi = 0.03\Phi_0$ . On the other hand, at such a small flux, the transmittance  $T_{\alpha, \alpha+2}$  (that hops over a lead) gets rather large values in some energy ranges affecting the quantum Hall effect; the implications will be discussed below.

The transmittances calculated according to Eq.(8) are illustrated in Fig.9. In Fig.9a, the plot of  $T_{12}^\uparrow$  and  $T_{21}^\downarrow$  prove the symmetry  $T_{12}^\uparrow(E) = T_{21}^\downarrow(-E)$  expressed by Eq.(9). The two transmittances allow an easy identification of the topological gap in the middle of the energy-axis (approximately in the range  $E \in [-0.25, 0.25]$ ), where  $T_{12}^\uparrow = T_{21}^\downarrow = 1$ , denoting the presence of two channels of opposite spin running in opposite directions, i.e., the well-known condition for QSHE.

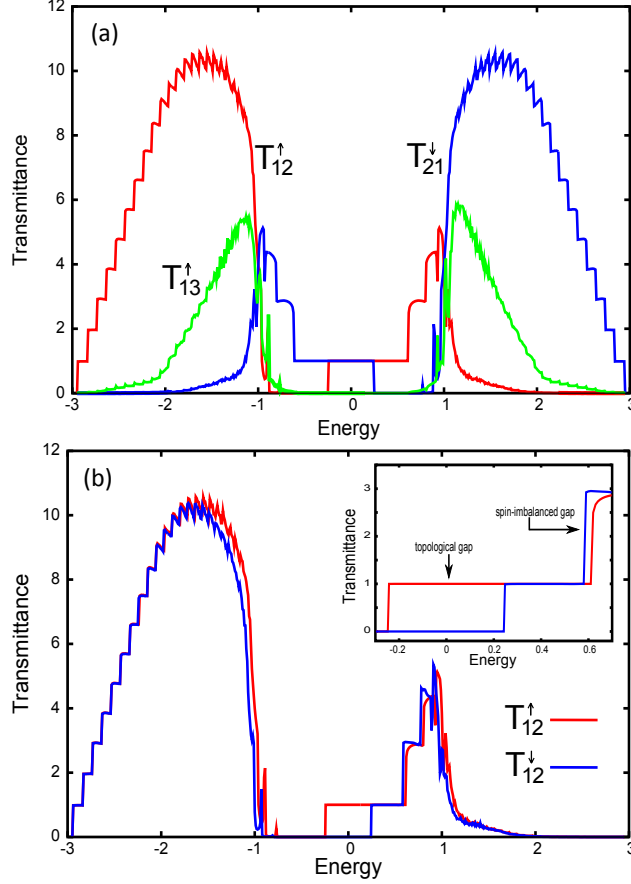


FIG. 9: (Color online) (a) Illustration of the symmetry  $T_{12}^{\uparrow}(E) = T_{21}^{\downarrow}(-E)$ ; the transmittances show plateaus corresponding to all gaps present in the spectrum.  $T_{13}$  is symmetric around  $E = 0$  and vanishes in the topological and relativistic regions, but it is not negligible in the rest of the spectrum. (b)  $T_{12}^{\uparrow}$  and  $T_{12}^{\downarrow}$  coincide at high energies, but are shifted in the middle of the spectrum. The inset shows the topological gap, where  $T_{12}^{\uparrow} = 1$ ,  $T_{12}^{\downarrow} = 0$ , and the imbalanced-gap, where  $T_{12}^{\uparrow} = 1$ ,  $T_{12}^{\downarrow} = 3$  ( $\Phi = 0.03\Phi_0$ ,  $\lambda_{SO} = 0.05$ , number of sites is  $105 \times 40$ ).

In Fig.9b we compare the transmittance  $T_{12}^{\uparrow}$  with  $T_{12}^{\downarrow}$ , which carry the opposite spin but runs in the same direction. The two curves coincide at high energy, however they show a significant shift in the central region of the spectrum. This shift of the transmittances is an obvious consequence of the shifted spin-dependent energies in the spectrum, which has been already noticed in Fig.5. The inset depicts the energy range that comprises the topological gap and the spin-imbalanced gap about  $E = 0.6$ , where we have to realize that  $T_{12}^{\uparrow} = 1$  and  $T_{12}^{\downarrow} = 3$ . As the other transmittances vanish, we may conclude that in this gap there are four active channels, one of spin-up and three of spin-down, all of them running in the same



direction. In the next subsection, when calculating the transverse resistance, we shall see that this spin-imbalance yields unusual plateaus of both integer and spin Hall effect.

The relatively small value of the magnetic flux, at which we are compelled to perform the transport calculations, makes it interesting to discuss the behavior of  $T_{\alpha,\alpha+2}^\sigma$ . We remind that at strong magnetic fields, the gaps corresponding to the quantized plateaus are characterized by  $T_{\alpha,\alpha+1}^\sigma = \text{integer}$ , while all the other transmittances vanish, including  $T_{\alpha,\alpha+2}^\sigma$ . At such strong fields, the edge states are localized very close to the perimeter of the plaquette, and the negligible value of  $T_{\alpha,\alpha+2}$  may be considered as a measure of the high degree of edge localization. For  $\Phi = 0.03\Phi_0$  the transmittance  $T_{13}^\uparrow$  is shown in Fig.9a. One notices the vanishing of  $T_{13}$  in the topological gap, fact that attests the strong localization of the helical edge states. On the other hand, the large values shown in a rather wide range about  $E = \pm 1$  can be associated with the bulky character of the quantum states, accompanied by the absence of quantum plateaus in the corresponding energy range.

## B. Longitudinal and transverse charge and spin conductances

Without spin-flip processes, the system behaves as a two independent spin fluids. Then, the particle current in a multi-lead device can be written in the linear approach as  $I_\alpha^\sigma = \sum_{\beta\sigma} T_{\alpha\beta}^\sigma V_\beta^\sigma$ , where  $\{\alpha, \beta\}$  stand for the lead indices,  $I_\alpha^\sigma$  is the current through the lead  $\alpha$  and  $V_\beta^\sigma$  is the potential at the contact site  $\beta$ . Summing up the contributions of the two spin, the total charge- and spin-currents flowing through the lead  $\alpha$  read:

$$I_\alpha^Q = \frac{e^2}{h} \sum_\sigma I_\alpha^\sigma, \quad I_\alpha^S = \frac{e}{4\pi} \sum_\sigma \sigma I_\alpha^\sigma. \quad (10)$$

Since the transmittance matrix  $T_{\alpha,\beta}^\sigma$  is already known, the spin-resolved longitudinal and Hall resistances can be calculated according to the Landauer-Büttiker formalism as:

$$\begin{aligned} R_L^\sigma &= R_{14,23}^\sigma = (T_{24}^\sigma T_{31}^\sigma - T_{21}^\sigma T_{34}^\sigma)/D, \\ R_H^\sigma &= (R_{13,24}^\sigma - R_{24,13}^\sigma)/2 = (T_{23}^\sigma T_{41}^\sigma - T_{21}^\sigma T_{43}^\sigma - T_{32}^\sigma T_{14}^\sigma + T_{12}^\sigma T_{34}^\sigma)/2D, \end{aligned} \quad (11)$$

where  $D$  is any 3x3 subdeterminant of the transmittance matrix.

The comparative study of the Hall resistance, with and without SO coupling, is instructive. This is done in Fig.10a,b where  $R_H^\sigma$ , calculated at the flux  $\Phi = 0.03$ , is superimposed over the corresponding Hofstadter spectrum. When the spectrum and the resistance are

spin independent (the case  $\lambda = 0$ ), the two quantities look like in Fig.10a, where the antisymmetry  $R_H^\sigma(E, \Phi) = -R_H^\sigma(-E, \Phi)$  is obvious. If  $\lambda \neq 0$ , the previous antisymmetry at the reflection  $E \rightarrow -E$  is lost since one has now to inverse also the spin. Indeed, from Eq.(9) and Eq.(11), it follows immediately that  $R_H^\sigma(E, \Phi) = -R_H^{-\sigma}(-E, \Phi)$ .

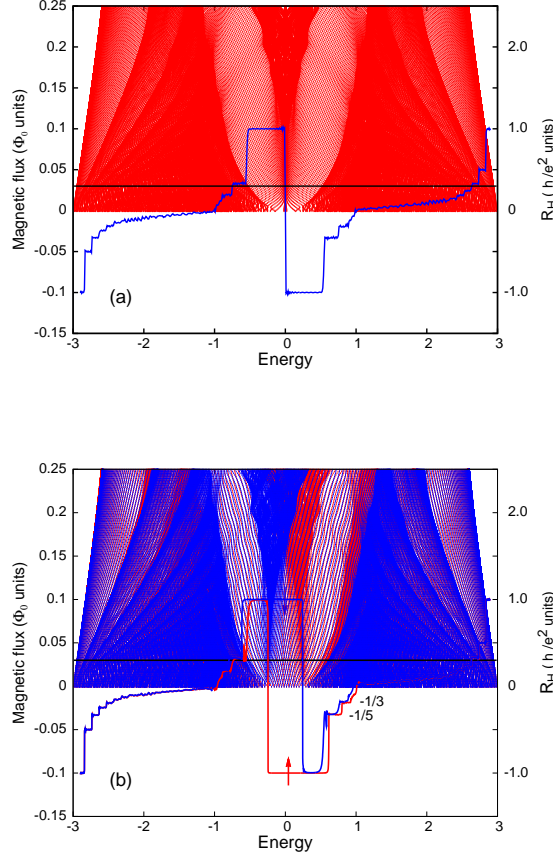


FIG. 10: (Color online) The spin-resolved Hall resistances  $R_H^\sigma$  at  $\Phi = 0.03$  (the flux is indicated by the black horizontal line): (a) at  $\lambda_{SO} = 0$ , the two resistances for spin up and down coincide and are symmetric around  $E = 0$ . (b) at  $\lambda = 0.05$ ,  $R_H^\uparrow$  (red curve) and  $R_H^\downarrow$  (blue curve) are different, and satisfies the property  $R_H^\uparrow(E) = -R_H^\downarrow(-E)$  mentioned in the text; the difference is more visible in the central region  $E \in (-1, 1)$ . Notice that the plateaus at  $\pm e^2/h$  cover the topological and first relativistic gap, confirming the behaviour of edge states sketched in Fig.6. The plaquette consists of  $33 \times 30$  sites.

It is to emphasize that in Fig.10b the spin-dependent Hall resistances shows the plateaus  $R_H^\downarrow = 1$  and  $R_H^\uparrow = -1$ , respectively, which extend over both the topological gap and the

the first relativistic gap, each one crossing the band of opposite spin. This behavior of the resistance is the immediate result of the fact that the chiral edge states located in the first relativistic gap extend also in the topological gap, as underlined in the previous section and observable in Fig.3(right).

Since the two spins act as two parallel channels, the total charge and spin resistances ( $R^Q$  and  $R^S$ , respectively) are given by:

$$\frac{1}{R_{L,H}^Q} = \frac{1}{R_{L,H}^\downarrow} + \frac{1}{R_{L,H}^\uparrow}, \quad \frac{1}{R_{L,H}^S} = \frac{1}{R_{L,H}^\downarrow} - \frac{1}{R_{L,H}^\uparrow}, \quad (12)$$

where the indices  $L$  and  $H$  stand for longitudinal and transversal (Hall), respectively. It is straightforward to prove the relationships:

$$R_H^Q(E) = -R_H^Q(-E), \quad R_H^S(E) = R_H^S(-E), \quad (13)$$

that show the different symmetries of the charge and spin resistance.

In the previous section, we mentioned the presence in the relativistic range of the energy spectrum of small gaps, induced by the spin-orbit splitting, where a spin imbalance exists. Obviously, the imbalance gives rise to  $R_H^\uparrow \neq R_H^\downarrow$ , and, in line with Eq.(12), this fact indicates the presence of a net spin current. In other words, the mesoscopic graphene plaquette exhibits QSHE not only in the weak topological gap, located symmetrically about  $E = 0$ , but also in some other energy stripes, where the number of spin-up edge states differs from the spin-down edge states. Another peculiar aspect is that, contrary to the situation in the topological gap, the two spins flow in the same direction, as the chirality of the edge states is the same no matter the spin.

The result of the numerical calculation for  $R_H^\uparrow$  and  $R_H^\downarrow$  is presented in Fig.11 together with the spin-dependent densities of states [33]. The shift between the spin-up and spin-down resistances, visible in the energy stripes about  $E \sim 0.6$  and  $E \sim 0.8$ , is confirmed by a similar shift between the two spin-dependent densities of states.

A last comment concerns the sign of the QSHE: in the topological gap one has  $R_H^\downarrow = 1$  and  $R_H^\uparrow = -1$ ; then, according to Eq.(12), the sign of the total Hall resistance  $R_H^S$  is positive. On the other hand, in the spin-imbalanced gap at  $E = 0.6$ , one has  $R_H^\downarrow = -1/3$ , and  $R_H^\uparrow = -1$ , meaning that  $R_H^S$  is negative. This opposite sign of  $R_H^S$  follows from the fact that, in the spin-imbalanced gap, the spin-up and spin-down edge states show the same chirality (which is not the case in the topological gap).

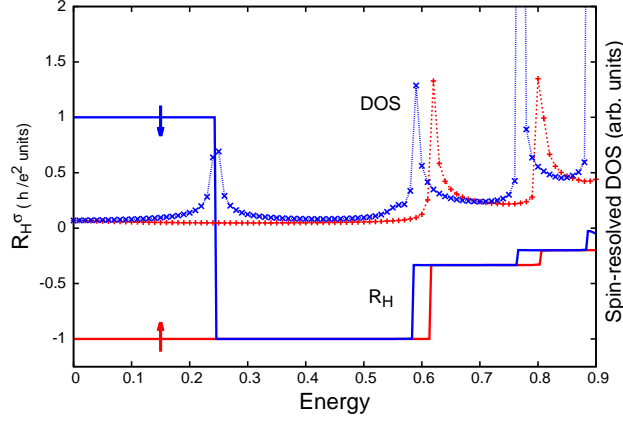


FIG. 11: (Color on line) The spin resolved Hall resistance and density of states; the shifted regions are those where the spin resistance should be non-zero. The densities of states exhibit the same shift ( $\Phi = 0.03$ ,  $\lambda_{SO} = 0.05$ , number of sites =  $105 \times 40$ ).

The longitudinal and Hall resistances being known from Eq.(12), in the spirit of the experimental work [1], we shall plot in Fig.12 the corresponding Hall conductances calculated as:

$$G_H^Q = \frac{R_H^Q}{(R_H^Q)^2 + (R_L^Q)^2}, \quad G_H^S = \frac{R_H^S}{(R_H^S)^2 + (R_L^S)^2}. \quad (14)$$

In what concerns the charge conductance  $G_H^Q$ , one has to observe not only the vanishing value in the topological range and the known plateaus at 2, 6 and 10 in the relativistic one, but also some unexpected plateaus at 4 and 8 (in units  $e^2/h$ ). A similar behavior is proved by the spin Hall conductance  $G_H^S$ , that shows the expected value  $2e/4\pi$  in the topological range, and then vanishes everywhere except the same energy stripes where the unusual values of the charge Hall conductance occur. In the respective stripes the spin Hall conductance equals  $-2e/4\pi$ . According to the previous discussions, it is obvious that they appear in the spin-imbalanced gaps generated by the intrinsic spin-orbit interaction in the presence of the magnetic field.

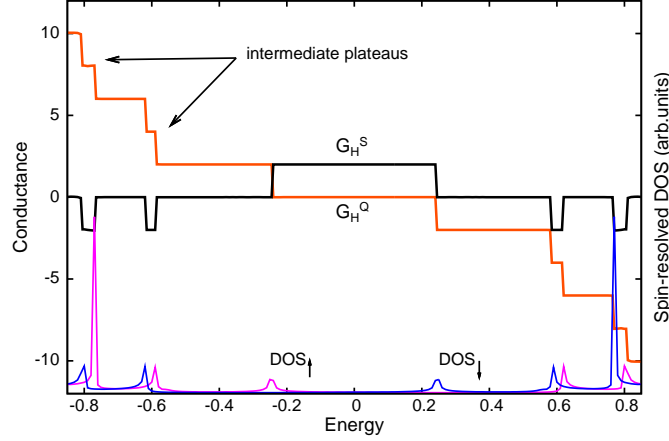


FIG. 12: (Color online) The spin and charge Hall conductance in the quantum regime (in  $2e/4\pi$  and  $e^2/h$  units, respectively): novel plateaus are visible in the imbalanced gaps opened by the intrinsic spin-orbit coupling. The spin-resolved density of states are also shown ( $\Phi = 0.03$ ,  $\lambda_{SO} = 0.05$ , number of sites =  $105 \times 40$ ).

#### IV. CONCLUSIONS

The main result consists in finding anomalous plateaus  $G_H^S = -2e/4\pi$  of the QSHE outside the topological gap, namely in the range of the *spin-imbalanced* gaps. In the same places, the IQHE exhibits also uncommon intermediate plateaus at  $G_H^Q = \pm(4e^2/h)(n+1)$ . The spin-imbalanced gaps are characterized by a non-equal number of spin-up and spin-down edge states. They are due to the splitting generated by ISO coupling, as sketched in Fig.6. Since we consider a small spin-orbit coupling ( $\lambda_{SO} \ll t$ ), this type of gaps appear in the relativistic range of the energy spectrum.

In the 'weak' topological gap, the degeneracy of the helical states is lifted by the magnetic field  $B$ . The states evolve with  $B$  and merge into the bands that confine the gap. During this process the states lose the edge character, as shown in Fig.4. At some higher magnetic fields, the topological gap gets filled with edge states of chiral origin, i.e., coming from the neighboring Dirac-Landau gaps. These states come also in pairs of opposite spin and chirality (see Fig.3(right)), so that the QSHE survives, and continues to equal  $2e/4\pi$ , even at higher magnetic fields, as long as the gap remains open.

We have noticed that, outside the topological gap, in the relativistic gaps of the energy spectrum, the degree of localization of the edge states depends on the spin. Moreover, the derivatives  $dE^\uparrow/d\Phi$  and  $dE^\downarrow/d\Phi$  are different, meaning that also the diamagnetic moments carried by states of opposite spins differ in magnitude.

We have looked for disorder effects on the topological gap and helical edge states at vanishing magnetic field. Although being robust at low disorder, the localization along the edges of the helical states is lost at higher disorder strength (see Fig.8a), when the states become of metallic-type, being distributed uniformly on the whole plaquette. We find also that the level spacing of the disordered helical states follow a Gaussian distribution at low disorder (see Fig.7b). For  $W \gtrsim 2$ , the topological gap at  $\Phi = 0$  becomes progressively narrower with increasing disorder under the compression of the levels that stem from the highly quasi-degenerated regions about  $E = \pm 1$ , resulting in a *tulip*-like spectrum (as in Fig.7a).

The transmittance matrix is spin dependent and its symmetries are shown in Eq.(9) and Fig.9a. The symmetry of  $T_{\alpha\beta}^\sigma(E, \Phi)$  results in the properties of the spin and charge Hall resistance of the four-lead graphene device, which we are interested in. The numerical calculations are performed at relatively small magnetic flux ( $\Phi = 0.03\Phi_0$ ) in order to catch the effect of all gaps specific to graphene (i.e., of Dirac-Landau and conventional Landau type). This allows also to show the energy dependence of  $T_{\alpha\alpha+2}^\sigma(E, \Phi)$ , the transmittance that kills the quantum plateaus when it takes large values (noticeable in Fig.9a).

## V. ACKNOWLEDGEMENTS

We acknowledge support from PNII-ID-PCE Research Programme (grant no. 0091/2011) and Core Programme (contract no. 45N/2009).

- 
- [1] K. S. Novoselov, A. K. Geim, S. V. Morozov, D. Jiang, M. I. Katsnelson, I. V. Grigorieva, S. V. Dubonos, and A. A. Firsov, *Nature* **438**, 197 (2005).
  - [2] C. L. Kane and E. J. Mele, *Phys. Rev. Lett.* **95**, 226801 (2005).
  - [3] C. L. Kane and E. J. Mele, *Phys. Rev. Lett.* **95**, 146802 (2005).
  - [4] B. A. Volkov and A. O. Pankratov, *Pis'ma Zh. Eksp. Teor. Fiz.* **42**, 145 (1985).

- [5] B. A. Bernevig, T. L. Hughes, S. C. Zhang, Science **314**, 1757 (2006).
- [6] M. König, S. Wiedmann, C. Brüne, A. Roth, H. Buhmann, L. W. Molenkamp, X. L. Qi, S. C. Zhang, Science **318**, 766 (2007).
- [7] C. Liu, T. L. Hughes, X.L. Qi, K. Wang, and S.C. Zhang, Phys. Rev. Lett. **100**, 236601 (2008).
- [8] L. Du, I. Knez, G. Sullivan, R. R. Du, arXiv:1306.1925 [cond-mat.mes-hall].
- [9] M. Z. Hasan and M. Z. Kane, Rev. Mod. Phys. **82**, 3045 (2010).
- [10] Y. Ando, J. of Phys. Soc. Japan **82**, 102001 (2013).
- [11] M. Gibertini, A. Singha, V. Pellegrini, M. Polini, G. Vignale, A. Pinczuk, L. N. Pfeiffer, and K. W. West, Phys. Rev. B **79**, 241406(R) (2009).
- [12] L. Tarruell, D. Greif, T. Uehlinger, G. Jotzu, and T. Esslinger, Nature **483**, 302 (2012).
- [13] C. Weeks, J. Hu, J. Alicea, M. Franz, and R. Wu, Phys. Rev. X **1**, 021001 (2011).
- [14] J. Balakrishnan, G. K. W. Koon, M. Jaiswal, A. H. Castro Neto, and B. Özyilmaz, Nature Physics **9**, 284 (2013).
- [15] M. Ezawa, J. Phys. Soc. of Jpn. **81**, 064705, (2012).
- [16] C. C. Liu, W. Feng, and Y. Yao, Phys. Rev. Lett. **107**, 076802 (2011).
- [17] L. Brey, H. A. Fertig, Phys. Rev. B **73**, 235411 (2006).
- [18] P. Delplace, D. Ullmo, G. Montambaux, Phys. Rev. B **84**, 195452 (2011).
- [19] O. Shevtsov, P. Carmier, C. Petitjean, C. Groth, D. Carpentier, and X. Waintal, Phys. Rev. X **2**, 031004 (2012).
- [20] W. Beugeling, N. Goldman, and C. M. Smith, Phys. Rev. B **86**, 075118 (2012).
- [21] In the continuous model for the graphene ribbon [3] the width of the gap at  $B = 0$  is  $\Delta = 6\sqrt{3}\lambda_{SO}$ , where  $\lambda_{SO}$  is the spin-orbit coupling constant.
- [22] Meaning  $E_a \neq E_b$  in Hamiltonian (2).
- [23] R. Rammal, J. Phys. France **46**, 1345 (1985).
- [24] N. Nemec and G. Cuniberti Phys. Rev. B **74**, 165411 (2006).
- [25] In the continuous model, the relativistic bands depend on the magnetic field as  $\sqrt{B}$ , while the conventional Landau bands are linear. For the finite plaquette described by the tight-binding model, this remains true at low magnetic flux, as it can be seen in Fig.3(left). The differences are due to the discrete lattice structure and to the confinement.
- [26] M. Niță, B. Ostahie, and A. Aldea, Phys. Rev. B **87**, 125428 (2013).
- [27] Another way to create such an imbalance is by imposing staggered energies of atoms A and

- B in the honeycomb lattice [20].
- [28] N. M. R. Peres, F. Guinea, and A. H. Castro Neto, Phys. Rev. B **73**, 125411 (2006).
  - [29] Another way to consider the spin-imbalance is by noting that the spin-orbit gap is an intersection of the first spin-up relativistic gap with the second spin-down relativistic gap. Then one has obviously  $N_{\uparrow} = 1$  and  $N_{\downarrow} = 3$ , i.e., the number of spin-up and spin-down edge states are different in the spectral range corresponding to the intersection.
  - [30] J. von Neumann and E. Wigner, Phys. Z. 30, 467 (1926).
  - [31] Yu. N. Demkov, P. B. Kurasov, Teoret. Mat. Fiz. **153**, 68 (2007).
  - [32] M. Niță, A. Aldea, and J. Zittartz, Phys. Rev. B **62**, 15367 (2000).
  - [33] The spin dependent DOS is defined as  $-(1/\pi)Im \sum_i G_{ii}^{\sigma}(E + i0)$ .